Two-scale modelling of fracture of magnesium phosphate cement under bending using X-ray computed tomography characterisation

Guosheng Zhang[a,b,c], Yue Li[a], Sadjad Naderi[b], Zigeng Wang[a,*], Mingzhong Zhang[b,*]

[a] Key Laboratory of Urban Security and Disaster Engineering of Ministry of Education, Beijing Key Laboratory of Earthquake Engineering and Structural Retrofit, Beijing University of Technology, Beijing, 100124, China

[b] Department of Civil, Environmental and Geomatic Engineering, University College London, London, WC1E 6BT, UK

[c] Department of Civil Engineering, Tsinghua University, Beijing 100084, China

Abstract: This paper presents an efficient experimental-numerical analysis of fracture mechanics in magnesium phosphate cement (MPC) based on the structural and mechanical properties of its constituents including potassium magnesium phosphate hexahydrate (MKP), magnesium oxide (MgO) and pores. At micro-scale, the fracture energy and material strength of solid phases were obtained relying on the combination of nanoindentation experiments and simulation. The X-ray computed tomography (XCT) image-based 3D meso-structure model of MPC beam was generated and incorporated with the finite element cohesive zone model to analyse the fracture process of MPC beam under three-point bending. The unknown fracture parameters of cohesive elements at the interface between MKP and MgO were determined via the model calibration process conditional to the experimental data in terms of relationship between macro-load and crack mouth opening displacement. The cohesive strengths obtained for MKP, MgO and MKP-MgO were found to be 5.8, 106 and 24 MPa, respectively. In the same order, the fracture energies were0.02, 0.08 and 0.04 N/mm , respectively.

Keywords: Magnesium phosphate cement; X-ray computed tomography; Nanoindentation; Damage evolution; Cohesive zone model.

1. Introduction

In comparison with ordinary Portland cement, magnesium phosphate cement (MPC) can better solidify harmful ions and heavy metals and contribute to the protection of ecosystem [1-3]. MPC also

* Corresponding authors. Email addresses: zigengw@bjut.edu.cn (Z. Wang); mingzhong.zhang@ucl.ac.uk (M. Zhang)

has other advantages, such as fast hardening, early-strength, high viscosity and so on [4-6]. Therefore, it has been widely used in civil engineering and other fields such as biomedical applications [7, 8], immobilization of heavy metals and nuclear wastes [9-11]. The growing use of MPC has been accompanied by growing concern over the mechanical characterisation [12-14]. Recently, some studies have been carried out to investigate the effects of molar ratio of MgO to KH_2PO_4, water-to-cement ratio, curing age and additives (e.g., fly ash and graphene oxide) on the material strength, microstructural properties, hardening and steel corrosion protectiveness [15-18]. The mechanical performance of MPC has been examined under different loading conditions such as compression, tension and bending [12, 19-21]. Among experimental methods, nanoindentation technology is one of the most advanced techniques to evaluate the micro-mechanical properties of such cementitious material. The previous studies revealed that it could be effectively linked to other experiments such as scanning electron microscope (SEM) [22, 23] and homogenisation methods [24-26] to obtain the properties of different phases, e.g., elastic modulus and hardness. Another common approach is three- or four-point bending test to characterise the flexural properties in different length scales from micro- to macro-level [27-29]. Normally, the fracture mechanism is analysed using the relationship between load and crack mouth opening displacement (CMOD). Along with all applicable experimental methods to determine the mechanical characteristics, X-ray computed tomography (XCT) can be utilised to provide more accurate information on micro/meso-structural characteristics and aid in, for example, the morphological analysis of crack during the entire fracture process [30, 31], which is experimentally difficult to be captured [32, 33]. An XCT-based model can be implemented in a modelling framework to explicitly represent the realistic structural features [34].

The mechanical properties of MPC depend on the heterogeneous, multiscale and multiphase structural characteristics that are influenced by many synthesis factors [18, 35]. These characteristics are an obstacle to fully understand the material behaviour. The heterogeneity is derived from a complex matrix-inclusion system, where numerous micro/meso-inclusions are formed with random tortuous, interconnected structures and particle-cluster aggregation. In some cases, it is difficult to distinguish the matrix among solid phases [36, 37]. To tackle the above-mentioned complexity from different perspectives, various experimental and numerical methods are required to be integrated into a systematic multiscale framework to accurately analyse the mechanical properties of MPC accounting for its real structural characteristics. However, the design of such a framework can also

be problematic due to high experimental/computational costs, large number of variables and complex links across different approaches in different length scales. Therefore, the choice of methods should be based on the objectives of characterisation while avoiding these issues.

To overcome the difficulties, this paper aims to develop a comprehensive, accurate, reliable, and cost-effective experimental-numerical technique to investigate the fracture-mechanical parameters of MPC based on its micro/meso-structure. The procedure proposed offers an uncomplicated solution to this complex problem with a minimum number of parameters. It allows to progressively determine the mechanical properties of constitute materials of MPC in two steps under nanoindentation at micro-scale and three-point bending loads at meso-scale. Fig. 1 outlines the strategy to implement the experimental and numerical methods proposed in an integrated framework. First, two types of MPC specimens are specifically fabricated for indention and bending tests. Then, the nanoindentation test is used to identify the elastic modulus, hardness and fracture energy for three main phases including magnesium oxide (MgO), potassium magnesium phosphate hexahydrate (MKP) as the main hydration product of MPC [38] and pores. Afterwards, the results are applied to a finite element (FE) analysis of the indentation process to determine the material strength. Before conducting the three-point bending test, the XCT technique is employed to reconstruct a real three-dimensional (3D) image and identify the structural characteristics like the volume fraction of each phase. In the bending test, the fracture mechanism is analysed in terms of force-crack opening response and the crack morphology using XCT after that. Finally, a cohesive FE model associated with the XCT image-based model is established, where the unknown input material parameters are indicated after the calibration using the experimental data. It should be noted that between the available modelling techniques, the cohesive zone model as one of the most extended ones has been broadly used because of its capability to simulate the realistic features of cracks [39-42].

2. Materials and sample preparation

2.1 Raw materials

The dead burned magnesia powder was calcined at 1600 °C for 6 h to achieve good crystallization properties: the purity of 91.7%, the average particle size of 23.3 μm and the specific area of 805.9 cm^2/g. The absolute and bulk densities are 3.46 and 1.67 g/cm^3, respectively. A summary of the chemical composition and physical properties of the calcined MgO are presented in Table 1, which was provided by Jinan Magnesia-Carbon Brick Plant Co. Ltd., China. Potassium dihydrogen

phosphate and borax used were produced by Beijing Chemical Plant, China in industrial grade with the purities more than 98% and 99.5%, respectively. Table 2 shows the mix proportion of MPC designed according to the previous studies [19, 21, 43].

2.2 Sample preparation

The MPC was poured into a mould with a size of 40×40×160 mm. Then, the beam-shape specimen was demoulded after 48 h to air-cure for 28 d at room temperature, 24 °C. For three-point bending test, a notch was cut at the middle of the lower part of the MPC beam with a width of 2 mm, a height of 10 mm, and a depth of 40 mm, as shown in Fig. 2. For nanoindentation test, a small cylinder with a diameter and height of about 5 mm was cut out from the beam. It is important to achieve a perfect surface for an accurate experimental analysis [44, 45]. For this, the cylindrical specimen was immersed in epoxy resin in a vacuum and then carefully polished with 400 mesh to 4000 mesh sandpaper, canvas and silk successively (Fig. 3). The surface roughness of the polished surface was checked using an atomic force microscope to ensure the roughness value was less than 100 nm. According to the XRD test, the main chemical components of MPC were hydrated products MKP and unreacted MgO. Based on the quantitative analysis of XRD results by the Rietveld method [46], the volume fractions of MKP and MgO were 42% and 58%, respectively. The volume ratio of MKP to MgO was 1: 0.714 [47].

3. Determination of material properties

3.1 Nanoindentation test

In this study, the nanoindentation tests were performed using an Agilent nanoindenter G200 testing system (Agilent Technologies, Santa Clara, California, USA) and a diamond Berkovich tip at room temperature, 24 ºC. The indentation process was carried out in three stages including loading (3 nm/s), holding (60 s) and unloading (3 nm/s). The maximum indentation depth was 2 μm and the minimum distance between indentation point was 20 μm. 100 indentation points were selected for testing.

For chemical mapping of the region of interest, a Quanta250 FEG scanning SEM equipped by an energy dispersive spectrometer (EDS) was used. The image resolutions of SEM and EDS were 3.5 nm and 130 eV, respectively. The atomic ratio of each indented region (IR) was analysed using EDS and labelled by the symbol describing the stoichiometry, e.g. IR_{MgO_3}. An example of indentation load-displacement curve for IR_{MgO_3} is shown in Fig. 4a. As seen in the figure, the characteristic points of the curve can be indicated by the maximum indentation load P_m (625 mN), the depth at the

beginning of the holding segment h_l (2000 nm), the maximum indentation depth h_m (2125 nm), the residual depth after unloading h_f (1353 nm) and the effective contact depth h_c (1550 nm) indicated by a line with the slope of unloading curve at (P_m, h_m). Fig. 4b illustrates the corresponding SEM image for IR_{MgO_3}.

The mechanical properties including the indentation modulus E and hardness H can be calculated form the unloading part of the load-depth curve using the Oliver and Pharr method [48].

3.2 Determination of fracture energy

Based on the energy method, if the heat loss is neglected during the indentation process, the fracture energy of W_c can be expressed as [49]:

$$W_c = W_T - W_P - W_E \tag{1}$$

where the subscripts T, E and P indicate the total, elastic and pure plastic energies.

For a smooth indentation load-displacement curve shown in Fig. 4a, it is possible to obtain the total and elastic energies. The total area under the loading and holding parts of the load-depth curve equals to W_c while the area below the unloading segment represents the elastic recovery of the material. However, the plastic term of W_P remains unknown as it cannot be explicitly calculated based on the load-displacement curve. According to a hybrid experimental-numerical analysis, it was suggested that the ratio of the pure-plastic to the total energy may be calculated by the functions of the characteristics of the load-depth curve [50]. For this, it is assumed that the curve at each stage is described as:

$$\begin{cases} P = \omega_m h^m & 0 \le h \le h_l \quad (Loading) \\ P = P_{m,} & h_l \le h \le h_f \quad (Holding) \\ P = \omega_n \left(h - h_f\right)^n & h_f \le h \le h_m \quad (Unloading) \end{cases} \tag{2}$$

where m and n represent the power exponents, and ω_m and ω_n are adjustment parameters that depend on the maximum load and the curve shape.

These parameters can be obtained by fitting experimental load curves. The two energy parameters are expressed as follows:

$$V_t = \frac{m+1}{2}, \qquad V_e = \frac{n+1}{2} \tag{3}$$

Based on Eqs. (3)-(5), the fracture energy can be obtained as:

$$W_c = \frac{V_t\left(1-\frac{h_f}{h_m}\right)}{V_e\left(2V_t-(2V_t-1)\frac{h_l}{h_m}\right)}W_T - W_E \quad (4)$$

Based on the linear elastic fracture mechanics theory [51], the critical energy release rate of G_c can be determined by:

$$G_c = \frac{W_c}{A_c} \quad (5)$$

$$A_c = C_0 h_c^2 \quad (6)$$

where C_0 is a factor related to the shape of indenter which is equal to 24.5 for Berkovich tip, and h_c is the effective contact depth that can be estimated as:

$$h_c = h_m - \epsilon\frac{P_m}{S} \quad (7)$$

where ϵ is a constant depending on the geometry of the indenter ($\epsilon = 0.75$ for a paraboloid of resolution).

A summary of material properties obtained from the nanoindentation tests and the results of EDS analysis performed is given in Tables 3 and 4 for MgO and MKP, respectively. The average energy release rates of MgO and MKP are 79 N/m and 20.4 N/m, respectively. The above material properties based on the nanoindentation tests can be used as the material input parameters of finite element simulation. Henceforth, it should be noted that the term "fracture energy" is used for "average energy release rate".

3.3 Finite element simulation

Heretofore, the elastic modulus, hardness and fracture energy have been obtained. To identify the material strength, the results of nanoindentation tests and the empirical-based method were incorporated in the calibration of FE model. The main idea behind the present approach is to compare the simulated force-displacement curve against the experimental data until a good match is achieved.

The FE model was established in ABAQUS software using the quasi-static (dynamic) explicit method. The specimen was simulated as a homogeneous cylinder with a radius of 40 μm and a height of 20 μm. The dimensions of the cylinder were large enough to be consistent with the standard Oliver-Pharr nanoindentation analysis that assumed the specimen was semi-infinite. As shown in Fig. 5a, the tip of Berkovich indenter was modelled with a height of 3.3 μm and the included angle of 65.3°. Both the specimens and the indenter were meshed using the element with a characteristic length of 0.4 μm.

The element types were hexahedral element (C3D8R) for specimens and rigid tetrahedral element (R3D4) for the indenter. The element length was set according to the results of previous studies on the mesh sensitivity for the similar models [52-54]. The bottom of the specimen was clamped while the top part was subjected to the indentation load by applying a small incremental vertical displacement of the indenter (Fig. 5b). The maximum displacement of 2 μm was prescribed in a long enough time (10^{-8} s) to be compatible with the quasi-static conditions. To measure the indentation depth, a reference point was set at the node located on the indenter tip.

The tip was considered as a rigid body as its deformation is negligible in compassion with the specimen during the indentation process. For the specimen, an ideal elastoplastic material model was assigned. Such a model requires few input parameters while it can accurately predict the mechanical behaviour and reduce the complexity. The efficiency of this material model is demonstrated through the discussion on the simulation and experimental results later. The elastic parameters were previously acquired (Tables 3 and 4). The densities of MgO and MKP are 3.54 and 1.864 g/cm^3, respectively [34, 55]. The only unknown parameter was yield stress, which can be obtained based on the experimental results for incompressible materials. According to the experimental results, it was shown that the hardness of elastoplastic materials could be a function of the yield stress σ_y [56]. Therefore, here, for the sake of simplicity, the overall relationship is assumed as:

$$H = \alpha\sigma_y \tag{8}$$

where α is a coefficient that can be determined through the FE model calibration process conditional to the experimental results.

3.4 Determination of material strength

First, different values were given to the parameter α to calculate the corresponding yield stress for both models of MgO and MKP. Then, a comparison of force-displacement data between experiment and simulation was conducted for the given parameters. The initial estimation of the range of α was made based on trial and error. Thereafter, α was gradually changed within the range to find the best-fitting results. In Fig. 6a and b, the indentation load-displacement curves are shown for different values of α for MgO (12-18) and MKP (16-22), respectively. As seen, the simulation results corresponding to the values 15 and 19 are in good agreement with the experimental data for MgO and MKP, respectively. The corresponding yield stress σ_y and the relative errors are presented in Table 5 regarding the characteristic points of load-displacement curve. Moreover, Fig. 6c depicts the

example of simulated morphology of indentation imprints observed for both cases of MgO and MKP, which is similar to the SEM image of the tested sample illustrated in Fig. 4b. The matrix region in contact with the indenter was subjected to large compression deformation. It can be interpreted that the compressive mode was a dominant regime during the indentation process. So, the value of yield stress can be a good estimation of the uniaxial compressive strength [57-59]. The elastic modulus, fracture energy and material strength obtained from nanoindentation test and FE simulation were used for the estimation of material parameters in the simulation of three-point bending test below.

4. X-ray CT imaging and three-point bending test

4.1 X-ray CT image processing and analysis

The MPC beam was scanned by the nanoVoxel 4000 series high-resolution industrial CT (Sanying, China) with the working voltage of 190 kV, the current of 120 mμA and the exposure time of 0.70 s. 900 projections were obtained during a rotation of 360°, corresponding to a rotation step of 0.4° and the scanning size of 1120×1120 pixels. The spiral CT scan of each beam produced a sequence of 4480 two-dimensional (2D) CT slices.

The XCT images were imported to AVIZO software [60] for processing based on the watershed method. After that, a dimensional model of the scanned physical zone of the sample was developed, which resulted in the 3D image stacks consisting of cubic voxels of 3.33×3.33×3.33 μm^3. Fig. 7a shows the reconstructed 3D image of the scanned zone of the beam sample before three-point bending test. In the reconstruction process, the 8-bit greyscale was selected to express the signal intensity of the components detected by the charged-coupled device (CCD) camera, the value of which ranged from 0 (black) to 255 (white). The pore phase appears as black voxel in the reconstructed image since it almost does not absorb the X-ray, as seen in Fig. 7b. On the contrary, other phases (i.e., MgO and MKP) have high density and absorb most of the X-ray emission and therefore, they appear as the bright voxels in the image. As the density of MgO is about 2 times of that of MKP, it can be interpreted that the light grey voxels represent MgO and the dark grey ones stand for MKP.

To reduce the computational cost, the middle part of the beam with a width of 20 mm was only considered as the region of interest (ROI), where the main fracture surface was formed in three-point bending test. As one of the most common approach, the tangent-slope grey-level thresholding method proposed by Scrivener [61] was applied to segment different phases. Fig. 8 illustrates the grey level distribution of the original image, where the numbers of voxels are relatively larger between 100 and

180. To estimate the upper threshold value for the porosity, the turning point (T1) was used, where the slope of the frequency curve drastically changed. The grey level of 132 at this point represented the pore/solid threshold value. A threshold value of 153 (T2) was selected to achieve the same volume fraction of MgO to MKP (1:0.714) obtained from XRD analysis. The output of image segmentation was a set of 1120 ternary images. The data of each phase was stored separately as tagged image format (TIFF). Fig. 9 illustrates an example of the original 2D XCT image versus segmented one. The segmentation process was carried out before and after three-point bending test, the obtained data from which were used in the experimental analysis of cracks and FE simulation.

4.2 Three-point bending test

The three-point bending test of MPC beam was conducted using the WEW-300 tensile and compression testing machine according to ASTM C293/293M [30, 62]. The sample was restrained using pin and roller supports near the ends of the beam, as demonstrated in Fig. 2. The test was carried out by statically imposing a displacement rate of 0.02 mm/min. A 100 kN type C1 HBM load cell was mounted on an INSTRON 1195 electromechanical testing machine. To measure CMOD, a TML resistive full bridge transducer was used astride the notch. The data acquisition and signal control were carried out using the HBM Spider 8 control unit.

Fig. 10 shows the force-CMOD curve which is similar to that of typical cementitious materials. During the loading process, the curve can be divided into three segments including the elastic region before Point I, the pre-peak behaviour between Point I and Point II (the maximum load) and the softening branch following Point II. Based on the curve, the value of elastic stiffness can be obtained, which was equal to 8.4×10^7 N/m. The maximum load and the corresponding value of CMOD were found to be 2.05 kN and 0.032 mm, respectively. At the end of loading, the maximum displacement and the fracture energy were found to be 0.18 mm and 123.5 mJ, respectively. Fig. 11a illustrates the 3D morphology of the final crack in the ROI of notched MPC beam through the solid phase. The fracture surface was located between the top of notch and the upper part of beam almost parallel to the loading direction. For a better demonstration of damage growth mechanism in relation to mesostructure, Fig. 11b shows the crack path through the segmented phases. As observed in the figures, the cracks tended to propagate by connecting the neighbouring pores and evolve through MKP that was the weakest phase. The force-CMOD and the morphology of fracture surface were used for validation and comparison of the numerical approach below.

5. Meso-scale modelling of three-point bending

A cohesive FE model was developed based on the mesostructure generated by the XCT image processing and the mechanical properties obtained from the experimental-numerical analysis of nanoindentation. The model development was performed in the main four steps. First, the voxel-based mesostructure of ROI of MPC was converted to a FE model composed of solid elements. Second, the zero-thickness cohesive elements were inserted between the solid elements. Third, the generated solid/cohesive element mesh was exported to ABAQUS/Explicit for the simulation of behaviour of MPC beam under three-point bending. In this step, the full structure of MPC beam was constructed by merging the heterogeneous-mid part and the homogeneous-side parts. Forth, the input parameters of material properties were calibrated conditionally on the experimental data.

5.1 Generation of mesostructure mesh

The voxel-based model was generated from the TIFF image stack using ImageJ software [63]. The output data were used for the generation of mesostructure mesh using a MATLAB code including four main modules. The key steps of the process to generate mesh structure is shown using a flowchart in Fig. 12. The first module organises the data in a matrix, where each row contains the data of each voxel and the number of each row is considered as the identification (ID) number of each voxel. In the matrix, the first to the third column represent the corresponding position of voxel centre on the Cartesian coordinates and the fourth column indicates the phase ID number, i.e., 0 for pore, 1 for MKP and 2 for MgO. This data structure facilitates programming the second module for the conversion of voxels to hexahedral elements. In the conversion method, the nodal positions were calculated using the position of voxel and the uniform voxel size of 0.036 mm. The element connectivity and the global node numbers were indicated based on the voxel numbering progression. Accordingly, the matrices of node coordinates and solid elements were generated. As the pore phase was simulated as an empty space in the FE analysis, the corresponding elements were removed from the model. The third module was coded for insertion of cohesive elements through the solid mesh structure following three main steps: (1) The neighbouring elements were specified for each element based on shared nodes. (2) The coordinates of nodes of each element were duplicated from the original nodal matrix and sequentially stored into a new matrix, which changed the node numbering, and consequently the element connectivity should be updated, i.e. the solid elements were detached from each other. (3) The new matrices of nodes and elements were used to generate the so-called

cohesive interface element (CIE) as an 8-node rectangular prism element with zero thickness, as demonstrated in Fig. 13a. The method of sharing nodes between the CIE and the mutual faces of two neighbour hexahedral elements is schematically illustrated in Fig. 13b. After this step, all the hexahedral elements were reconnected through the CIEs. It should be mentioned that the orientation of CIEs must be consistent with the orientation of hexahedral elements for the right connection in the finite element mesh structure. The CIEs generated needed to be tagged with an ID number in the array data. Like hexahedral elements, the nodal connectivity of CIEs was stored in an individual matrix with nine columns (8 for the nodes and 1 for the ID number). Here, CIE-1, CIE-2 and CIE-12 were used for the elements inserted into MKP-MKP, MgO-MgO and MKP-MgO interfaces.

In the fourth module of the code, the matrices of the duplicated nodes, the updated hexahedral elements and the CIEs were used to generate an input file to ABAQUS with INP format. The keyword of COH3D8 was used for the cohesive elements. The elements sets were created based on the element types and the material ID numbers.

5.2 Boundary conditions of full domain

In the FE model, the MPC beam was composed of the heterogenous-mid part developed in the previous step and the homogenous-side parts as shown in Fig. 14. In the side parts, the equivalent of material properties of MPC was used. Such division of MPC beam allows to reduce the computations while accurately simulating the cracking process accounting for the mesostructural effect in the ROI as the major fracture zone [41]. The homogenous parts were also meshed with the hexahedral elements and the nodes were shared at the interfaces with the mid part to achieve a continuous mesh through the entire beam. The boundary conditions of MPC beam were set to be same as the experiment (Fig. 2). A quasi-static displacement load was applied with a maximum of 0.18 mm and a rate of 2 mm/s. Regarding the material models assigned, in the following, the method to calculate the homogenised mechanical properties of the side part is introduced and then the cohesive constitutive law proposed for the mid part is described.

5.3 Homogenised mechanical properties

It was assumed that the side-parts of the beam behaved like a linear elastic material with no damage. The equivalent elastic parameters can be obtained based on the volume fractions and the elastic properties of mesostructural components. The bulk modulus k and the shear modulus μ of each

phase were first calculated using their following relationships with elastic modulus E and Poisson's ratio ν, which are valid for incompressible materials [64]:

$$k = \frac{E}{3(1-2\nu)} \tag{9}$$

$$\mu = \frac{E}{2(1+\nu)} \tag{10}$$

Afterwards, the equivalent modulus of MPC can be calculated by the formulas derived using the self-consistent method for the complex composites in [65] as follows:

$$\bar{k} = k_2 + \sum_{r=0}^{1} \frac{q_r(k_r - k_2)(3\bar{k} + 4\bar{\mu})}{3k_r + 4\bar{\mu}} \tag{11}$$

$$\bar{\mu} = \mu_2 + \sum_{r=0}^{1} \frac{5q_r\bar{\mu}(\mu_r - \mu_2)(3\bar{k} + 4\bar{\mu})}{3\bar{k}(3\bar{\mu} + 2\mu_r) + \bar{\mu}(2\bar{\mu} + 3\mu_r)} \tag{12}$$

where the bar superscript denotes equivalent parameters, the subscript r indicates the variables related to the inclusion phases (i.e., where equal 0 and 1 are the ID numbers of pore and MKP, respectively) and the subscript number 2 denotes the matrix properties (i.e., the ID number of MgO), and q_r is the volume fraction of phase r.

It should be reminded that it is difficult to determine the matrix phase in MPC with such a complex structure. But MgO was considered as the matrix due to its relatively larger volume fraction and other phases as inclusions. For better measuring the volume fraction, the MPC beam was subdivided into several cubic cell units with the side length of 10 mm. By averaging 50 samples, the volume fraction of the phases of pores, MKP and MgO was found to be 7.92%±1.2%, 37.49%±3.3% and 53.98%±2.7%, respectively. After calculations of $\bar{k}$ and $\bar{\mu}$, the equivalent elastic modulus $\bar{E}$ can be determined as:

$$\bar{E} = \frac{9\bar{k}\bar{\mu}}{3\bar{k} + \bar{\mu}} \tag{13}$$

By inputting all the experimental results into Eqs. (11)-(15), $\bar{E}$ can be obtained as 58.4 GPa, where the mechanical properties of pores were set to 0 and the equivalent Poisson's ratio $\bar{\nu}$ was assumed to be 0.22 like MKP and MgO.

The applicability of the proposed self-consistent (SC) method to MPC specimen was assessed using the experimental data presented in [34]. The elastic modulus at the indentation point and the macroscopic elastic modulus of MPC were calculated using the SC method. The difference between the calculated and measured elastic moduli was found to be only 1.6%, indicating the accuracy of SC

method. However, it is worth mentioning that it might be possible to use another simpler homogenisation method like the weighted average approach since the overall structural response of MPC beam would be less sensitive to the mechanical properties of the side parts [66].

5.4 Cohesive constitutive law and material parameters

In the FE cohesive zone model, the elastic properties of MKP and MgO were assigned to all the hexahedral elements whereas the damage variables were defined for cohesive elements. The theory regarded to the constitutive response of cohesive elements has been repeatedly described in the literature [67, 68] and ABAQUS User's Manual [69]. Therefore, the key model configurations were merely pointed out here.

For the cohesive elements, the linear elastic traction-separation relationship was selected if followed by the nucleation and the linear evolution of damage according to the quadratic nominal stress criterion and fracture energy. It meant that a crack initiated when the quadratic interaction function was fulfilled as follows:

$$\left\{\frac{\langle t_n \rangle}{t_{n0}}\right\}^2 + \left\{\frac{t_s}{t_{s0}}\right\}^2 + \left\{\frac{t_t}{t_{t0}}\right\}^2 = 1 \tag{14}$$

where t_n, t_s and t_t represent the normal traction and two tangential tractions (shear cohesion), respectively, t_{n0}, t_{s0} and t_{t0} denote the critical tractions for three modes, and $\langle\,\rangle$ is Macaulay bracket:

$$\langle x \rangle = \begin{cases} x, & x \geq 0\ (Tension) \\ 0, & x < 0\ (Compression) \end{cases} \tag{15}$$

In addition to tensile/shear strength t_0, the normal/tangential fracture energy G was specified to completely indicate the bilinear traction-separation law. Hence, the failure separation δ_f can be obtained according to:

$$G = \int_0^{\delta_f} t(\delta) d\delta = \frac{1}{2} t_0 \delta_f \tag{16}$$

To describe the linear softening evolution under the combined normal and tangential separation, the effective relative displacement δ_m and scalar damage D were used as given below:

$$\delta_m = \sqrt{\langle \delta_n \rangle^2 + {\delta_s}^2 + {\delta_t}^2} \tag{17}$$

$$D = \frac{\delta_{mf}(\delta_{m,max} - \delta_{m0})}{\delta_{m,max}(\delta_{mf} - \delta_{m0})} \tag{18}$$

where $\delta_{m,max}$ denotes the maximum effective relative displacement obtained during the loading, δ_{m0} and δ_{mf} represent the effective displacements at damage initiation and final failure, respectively, and D evolves monotonically from 0 (intact) to 1 (fully damage).

The stress components of the traction-separation model are affected by the damage as follows:

$$t_n = \begin{cases} (1-D)t_n^*, & t_n^* \geq 0 \\ t_n^*, & t_n^* < 0 \ (no\ damage\ to\ compressive\ stiffness) \end{cases} \qquad (19)$$
$$t_s = (1-D)t_s^*, t_t = (1-D)t_t^*$$

where the asterisk superscript indicates the traction-components predicted by the elastic traction-displacement behaviour for the current separation without damage.

The index of SDEG was selected to determine the overall damage as an output variable. Regarding the input parameters, the initial elastic stiffness of cohesive elements should be in the range of 20-50 times greater than the elastic modulus of solid element for bulk material with Poisson's ratio of 0.2 [70, 71]. A large enough value of stiffness enables avoiding artificial compliance, which would change the dynamic wave speed. On the other hand, the cohesive stiffness should not be very high since it may unnecessarily reduce the time step. Therefore, the elastic stiffness was set to 10^5 as a penalty coefficient for all CIEs in normal and tangential directions. For CIE-1 and CIE-2, the critical normal traction t_{n0} (i.e., uniaxial tensile strength) can be estimated approximately to be 1/10 of the compressive strength of MKP an MgO obtained in Section 4.2 [72]. Based on the previous studies [73, 74], it is possible to assume the critical shear tractions t_{s0} and t_{t0} to be equal to that of in normal directions. The parametric studies in [66] revealed that the strength of the sample is slightly increased by increasing the shear strength while the macro-crack morphology remains unchanged. Hence, while considering the lack of experimental data, it can be a reasonable approach to set the shear fracture properties as the same value as those in normal directions for all the CIEs. The fracture energy was assumed as the one obtained from the nanoindentation test. The density values of CIE-1 and CIE-2 and solid elements were equally adjusted while that of CIE-12 was assumed to be the average of densities of MgO and MKP. The values of critical traction and fracture energy regarding to CIE-12 remained unknown which were determined via the model calibration procedure based on the experimental data explained in the following section.

The choice of mesh size has a crucial influence on the simulation results. The sensitivity analysis was carried out to evaluate the influence of mesh size on simulation results in terms of force-CMOD

relationship and obtain the most suitable mesh size considering accuracy and computational efficiency. To achieve this, the CIE-12 was initially treated as CIE-1 and the mesh size was set as 0.14 mm, 0.12 mm, 0.1 mm, 0.08 mm, 0.06 mm, and 0.04 mm, respectively, while other parameters were kept constant. The simulated force-CMOD curves for different mesh sizes are shown in Fig. 15, indicating that the mesh dependence of the simulation results can be ignored when the mesh size is smaller than 0.1 mm. Thus, a mesh size of 0.1 mm was selected for the simulations below to improve the computational efficiency without losing the accuracy. It should be mentioned that such approach is only suitable for the simulation of MPC beams with a limited size of region of interest rather than full-scale beams that would result in too many elements for simulations and unacceptable computational costs.

5.5 Calibration method and simulation results

Like the nanoindentation model presented earlier, the main concept of the calibration method is to gradually change the parameters until the simulation results match the experimental data as closely as possible in terms of force-CMOD relationship. Although in this case, the parameters should be systematically changed due to two unknown variables.

The cohesive strength and fracture energy simultaneously contribute to the mechanical response of MPC beam during the loading process, which makes it difficult for uncoupling their effects on the force-CMOD curve. However, from another point of view, each parameter dominantly contributes to different loading stage. Therefore, it can be interpreted that t_{n0} has a significant influence on the maximum load [41] while G is dominant in the post-peak region [75]. From this perspective, the model was sequentially calibrated using the algorithm shown in Fig. 16. The CIE-12 was initially treated as CIE-1, i.e., the same properties were assigned. Then, the model was calibrated as a function of t_{n0}, which gradually varied in a range between those of CIE-1 and CIE-2 until the simulated maximum load got close to the test data point, i.e. 2.05 kN. If the softening part was fitted and so did overall curve, the model was calibrated. But if not, the value of t_{n0} obtained based on the previous step was applied in the model while G changed until the simulated post-peak behaviour matched the experimental curve.

For better understanding, Fig. 17a and b illustrate the effect of each parameter on the force-CMOD curve when the other was fixed. By increasing t_{n0} and G of the CIE-12, the peak load increased, and the post-peak behaviour became more ductile. These procedures were repeated until a

set of parameters led to the expected outcomes. Fig. 17c shows the best numerical results achieved in comparison with the test data points when $t_{n0} = 24$ MPa and $G = 0.041$ N/mm where the maximum standard deviation was 120 N. A summary of the material properties used in the final model is given in Table 6.

Moreover, the cohesive FE model based on XCT can simulate the real fracture morphology. Fig. 18 demonstrates the simulated fracture process in MPC beam is in good agreement with the experiment in term of morphology (Fig. 11). The fracture process in the mid-part of MPC beam is shown in Fig. 19 with the cross-sectional views corresponding to the different values of CMOD. The crack nucleated around the above notch and propagated towards the upper part of the beam when the CMOD was about less than 0.06 mm. The major crack opening occurred when CMOD reached about 0.08 mm. In the initial stage of loading, cracks tended to grow through the MKP phase with relatively weaker mechanical properties. To validate the model accuracy, the final crack in the corresponding 2D XCT slice is shown for comparison in Fig. 19.

Comparing Fig. 19e and f, it can be found that the simulated crack position is in good agreement with the crack position in the XCT slice. The cracks propagate from the vicinity of a hole in the lower incision to the upper right, and in the upper part, they pass through a relatively large pore. Under the three-point bending load, the crack initiated in the lower part of the beam and then grew upward. The width of the crack underneath was larger, which is consistent with the that observed in the experiment.

The XCT slice shown in Fig. 18f indicates the upper crack tended to be larger than that of the lower crack, which can be ascribed to the fact that the XCT scanning of the beam was conducted after three-point bending test and the beam had been broken into two parts at that moment. For XCT scanning, the two broken parts needed to be put together again, while it was difficult to fully eliminate the gap at the fracture surface. The gap at the top was larger than at the bottom when the two broken parts were put together by hands, leading to the result that the crack width in the lower part of the beam was smaller than the upper part.

6. Conclusions

In this paper, an integrated two-scale framework was presented based on the experimental-numerical method to characterise macro-fracture behaviour of MPC, accounting for its 3D mesostructure and mechanical properties of three constituents including MgO, MKP and pores. The mesostructural characteristics of the constituents were derived by X-ray computed tomography (XCT) and their

mechanical properties were found in two steps at micro- and meso-levels. First, based on the nanoindentation test coupled with the simulation technique, the elastic modulus, material strength and fracture energy were obtained for MgO as 286.7 GPa, 106 MPa and 0.079 N/mm, respectively, and in the same order for MKP as 29.4 GPa, 5.8 MPa and 0.02 N/mm, respectively. Second, the FE analysis of three-point bending of MPC beam was conducted using XCT image-based meso-structure model and calibrated conditionally to the experimental data to determine the remaining fracture parameters. The cohesive strength and fracture energy of CIE-12 elements were found to be 24 MPa and 0.041 N/mm, respectively, while the loading capacity of the beam and the maximum CMOD were obtained as about 2 kN and 0.18 mm, respectively.

It should be noted that the calibration method in the final stages did not only detect the properties for CIE-12 but also, in other ways, could implicitly compensate the approximations and the simplifications used for other input parameters, which would affect the model accuracy. Regarding other advantages, the method provided a fast convergence algorithm for this case and it did not need a large number of simulations (144 runs). However, the parameter characterisation might be more effective if the FE models were incorporated with a machine learning approach instead of the current calibration method to reduce the number of iteration of simulation [76-78].

Acknowledgements

The authors gratefully acknowledge the financial support from the Natural Science Foundation of China under Grant No. 51678011 and the Visiting Researcher Fund Program of State Key Laboratory of Water Resources and Hydropower Engineering Science, China under Award No. 2019SGG01 as well as the Engineering and Physical Sciences Research Council (EPSRC), UK under Grant No. EP/R041504/1 and the Royal Society, UK under Award No. IEC\NSFC\191417. Meanwhile, the authors would like to acknowledge the Avizo software package supported by Beijing Institute for Scientific and Engineering Computing, Beijing University of Technology.

Nomenclature

A	Contact area
CIE	Cohesive interface element
CIE-1, CIE-2, CIE-12	Elements inserted into MKP-MKP, MgO-MgO, MKP- MgO interface
CMOD	Crack mouth opening displacement

COH3D8	Hexahedral cohesive elements
C3D8R	Hexahedral solid element
XCT	X-ray computed tomography
D	Scalar damage
E	Indentation modulus
G_c	Critical energy release
H	Hardness
h_c	Effective contact depth
h_f	Residual depth after unloading
h_l	Depth at the peak load
IR	Indented region
$m,\ n$	Power exponents
MgO	Magnesium oxide
MKP	Potassium magnesium phosphate hexahydrate
MPC	Magnesium phosphate cement
P	Indentation load
P_m	Maximum indentation load
ROI	Region of interest
R3D4	Quadrilateral solid element
S	The contact stiffness
$t_n,\ t_s,\ t_t$	Normal traction and two tangential tractions (shear cohesion)
$t_{n0},\ t_{s0},\ t_{t0}$	Critical tractions for three modes
$V_t,\ V_e$	Energy parameters
$W_c,\ W_T, W_P, W_E$	Fracture, total, elastic and pure plastic energy
$\omega_m,\ \omega_n$	Adjustment parameters
k	Bulk modulus
μ	Shear modulus
ν	Poisson's ratio
γ	Correction factor

σ_y	Yield stress
α	Coefficient for relationship between the hardness and yield stress
δ_f	Failure separation
δ_m	Effective relative displacement

References

Uncategorized References

[1] S.A. Kulikova, S.E. Vinokurov, R.K. Khamizov, N.S. Vlasovskikh, B.F. Myasoedov, The Use of MgO Obtained from Serpentinite in the Synthesis of a Magnesium Potassium Phosphate Matrix for Radioactive Waste Immobilization, Applied Sciences, 11 (2021) 220.

[2] M.A. Haque, B. Chen, Research progresses on magnesium phosphate cement: A review, Construction and Building Materials, 211 (2019) 885-898.

[3] J.S. Li, X. Qiang, W. Ping, T.T. Zhang, Z. Ying, Comparison of solidification/stabilization of lead contaminated soil between magnesia–phosphate cement and ordinary portland cement under the same dosage, Environmental Progress & Sustainable Energy, 35 (2016) 88-94.

[4] S.A. Walling, J.L. Provis, Magnesia-based cements: a journey of 150 years, and cements for the future?, Chemical reviews, 116 (2016) 4170-4204.

[5] D. Wang, Y. Yue, T. Mi, S. Yang, Y. Bai, Effect of magnesia-to-phosphate ratio on the passivation of mild steel in magnesium potassium phosphate cement, Corrosion Science, 174 (2020) 108848.

[6] J. Li, W. Zhang, P. Monteiro, Mechanical properties of struvite-K: A high-pressure X-ray diffraction study, Cement and Concrete Research, 136 (2020).

[7] S. Yu, L. Liu, C. Xu, H. Dai, Magnesium phosphate based cement with improved setting, strength and cytocompatibility properties by adding Ca(H2PO4)2.H2O and citric acid, J Mech Behav Biomed Mater, 91 (2019) 229-236.

[8] M.A. Haque, B. Chen, In Vitro and in Vivo research advancements on the Magnesium Phosphate cement biomaterials: A review, Materialia, 13 (2020) 100852.

[9] L. Wang, L. Chen, B. Guo, D. Tsang, V. Mechtcherine, Red Mud-Enhanced Magnesium Phosphate Cement for Remediation of Pb and As Contaminated Soil, Journal of Hazardous Materials, (2020) 123317.

[10] L. Wang, I. Yu, D. Tsang, S. Li, J.S. Li, C.S. Poon, Y.S. Wang, J.G. Dai, Transforming wood waste into water-resistant magnesia-phosphate cement particleboard modified by alumina and red mud, Journal of Cleaner Production, 168 (2017) 452-462.

[11] D. Leng, X. Li, Y. Lv, H. Tan, N. Li, Z. Liu, W. Jiang, D. Jiang, Cesium immobilization by K-struvite crystal in aqueous solution: Ab initio calculations and experiments, Journal of Hazardous Materials, 387 (2020) 121872.

[12] Y. Li, W. Bai, T. Shi, A study of the bonding performance of magnesium phosphate cement on mortar and concrete, Construction and Building Materials, 142 (2017) 459-468.

[13] J. Qin, J. Qian, C. You, Y. Fan, Z. Li, H. Wang, Bond behavior and interfacial micro-characteristics of magnesium phosphate cement onto old concrete substrate, Construction and Building Materials, 167 (2018) 166-176.

[14] B. Jin, L. Chen, B. Chen, Factors assessment of a repair material for brick masonry loaded cracks using magnesium phosphate cement, Construction and Building Materials, 252 (2020) 119098.

[15] B. Xu, H. Ma, H. Shao, Z. Li, B. Lothenbach, Influence of fly ash on compressive strength and micro-characteristics of magnesium potassium phosphate cement mortars, Cement and Concrete Research, 99 (2017) 86-94.

[16] H. Tang, J. Qian, Z. Ji, X. Dai, Z. Li, The protective effect of magnesium phosphate cement on steel corrosion, Construction and Building Materials, 255 (2020) 119422.

[17] R. Liu, B. Pang, X. Zhao, Y. Yang, Effect of rice husk ash on early hydration behavior of magnesium phosphate cement, Construction and Building Materials, 263 (2020) 120180.

[18] D. Hou, H. Yan, J. Zhang, P. Wang, Z. Li, Experimental and computational investigation of magnesium phosphate cement mortar, Construction and Building Materials, 112 (2016) 331-342.

[19] Y. Li, J. Sun, B. Chen, Experimental study of magnesia and M/P ratio influencing properties of magnesium phosphate cement, Construction and Building Materials, 65 (2014) 177-183.

[20] Y. Li, Y. Li, T. Shi, J. Li, Experimental study on mechanical properties and fracture toughness of magnesium phosphate cement, Construction and Building Materials, 96 (2015) 346-352.

[21] Y. Li, B. Chen, Factors that affect the properties of magnesium phosphate cement, Construction and building materials, 47 (2013) 977-983.

[22] W. Wilson, J. Rivera-Torres, L. Sorelli, A. Durán-Herrera, A. Tagnit-Hamou, The micromechanical signature of high-volume natural pozzolan concrete by combined statistical nanoindentation and SEM-EDS analyses, Cement and Concrete Research, 91 (2017) 1-12.

[23] C. Hu, Z. Li, A review on the mechanical properties of cement-based materials measured by nanoindentation, Construction and Building Materials, 90 (2015) 80-90.

[24] Y. Li, P. Wang, Z. Wang, Evaluation of elastic modulus of cement paste corroded in bring solution with advanced homogenization method, Construction and Building Materials, 157 (2017) 600-609.

[25] J. Němeček, V. Králík, J. Vondřejc, Micromechanical analysis of heterogeneous structural materials, Cement and Concrete Composites, 36 (2013) 85-92.

[26] S. Liang, Y. Wei, Z. Wu, Multiscale modeling elastic properties of cement-based materials considering imperfect interface effect, Construction and Building Materials, 154 (2017) 567-579.

[27] I. Stavrakas, D. Triantis, S. Kourkoulis, E. Pasiou, I. Dakanali, Acoustic emission analysis of cement mortar specimens during three point bending tests, Latin American Journal of Solids and Structures, 13 (2016) 2283-2297.

[28] A. Lavrov, K. Gawel, A. Stroisz, M. Torsæter, S. Bakheim, Failure modes in three-point bending tests of cement-steel, cement-cement and cement-sandstone bi-material beams, Construction and Building Materials, 152 (2017) 880-886.

[29] H. Zhang, B. Šavija, S.C. Figueiredo, E. Schlangen, Experimentally validated multi-scale modelling scheme of deformation and fracture of cement paste, Cement and Concrete Research, 102 (2017) 175-186.

[30] J. Tejchman, Experimental investigations of damage evolution in concrete during bending by continuous micro-CT scanning, Materials Characterization, 154 (2019) 40-52.

[31] Y.-S. Wang, J.-G. Dai, Use of magnesia sand for optimal design of high performance magnesium potassium phosphate cement mortar, Construction and Building Materials, 153 (2017) 385-392.

[32] Z.-J. Yang, B.-B. Li, J.-Y. Wu, X-ray computed tomography images based phase-field modeling of mesoscopic failure in concrete, Engineering Fracture Mechanics, 208 (2019) 151-170.

[33] Q. Yu, H. Liu, T. Yang, H. Liu, 3D numerical study on fracture process of concrete with different ITZ properties using X-ray computerized tomography, International Journal of Solids and Structures, 147 (2018) 204-222.

[34] Y. Li, G. Zhang, Z. Wang, Z. Guan, Experimental-computational approach to investigate compressive strength of magnesium phosphate cement with nanoindentation and finite element analysis, Constr Build Mater, 190 (2018) 414-426.

[35] L. Mo, L. Lv, M. Deng, J. Qian, Influence of fly ash and metakaolin on the microstructure and compressive strength of magnesium potassium phosphate cement paste, Cement and Concrete Research, 111 (2018) 116-129.

[36] H. Ma, B. Xu, Z. Li, Magnesium potassium phosphate cement paste: degree of reaction, porosity and pore structure, Cement and Concrete Research, 65 (2014) 96-104.

[37] B. Xu, F. Winnefeld, J. Kaufmann, B. Lothenbach, Influence of magnesium-to-phosphate ratio and water-to-cement ratio on hydration and properties of magnesium potassium phosphate cements, Cement and Concrete Research, 123 (2019) 105781.

[38] H. Ma, B. Xu, J. Liu, H. Pei, Z. Li, Effects of water content, magnesia-to-phosphate molar ratio and age on pore structure, strength and permeability of magnesium potassium phosphate cement paste, Materials & Design, 64 (2014) 497-502.

[39] S. Nayak, N.A. Krishnan, S. Das, Fracture response of metallic particulate-reinforced cementitious composites: Insights from experiments and multiscale numerical simulations, Cement and Concrete Composites, 97 (2019) 154-165.

[40] E.A. Rodrigues, O.L. Manzoli, L.A. Bitencourt Jr, 3D concurrent multiscale model for crack propagation in concrete, Computer Methods in Applied Mechanics and Engineering, 361 (2020) 112813.

[41] W. Trawiński, J. Tejchman, J. Bobiński, A three-dimensional meso-scale modelling of concrete fracture, based on cohesive elements and X-ray μCT images, Engineering fracture mechanics, 189 (2018) 27-50.

[42] S. Naderi, M. Zhang, Meso-scale modelling of static and dynamic tensile fracture of concrete accounting for real-shape aggregates, Cement and Concrete Composites, (2020) 103889.

[43] Y. Li, T. Shi, J. Li, Effects of fly ash and quartz sand on water-resistance and salt-resistance of magnesium phosphate cement, Construction and Building Materials, 105 (2016) 384-390.

[44] G. Fang, M. Zhang, Multiscale micromechanical analysis of alkali-activated fly ash-slag paste, Cement and Concrete Research, 135 (2020) 106141.

[45] G. Fang, M. Zhang, The evolution of interfacial transition zone in alkali-activated fly ash-slag concrete, Cement and Concrete Research, 129 (2020) 105963.

[46] G. Le Saoût, V. Kocaba, K. Scrivener, Application of the Rietveld method to the analysis of anhydrous cement, Cement and concrete research, 41 (2011) 133-148.

[47] Y. Li, G. Zhang, Z. Wang, Z. Guan, Experimental-computational approach to investigate compressive strength of magnesium phosphate cement with nanoindentation and finite element analysis, Construction and Building Materials, 190 (2018) 414-426.

[48] W.C. Oliver, G.M. Pharr, An improved technique for determining hardness and elastic modulus using load and displacement sensing indentation experiments, Journal of Materials Research, 7 (2011) 1564-1583.

[49] J. Chen, Indentation-based methods to assess fracture toughness for thin coatings, Journal of Physics D: Applied Physics, 45 (2012) 203001.

[50] Q. Zeng, Y. Wu, Y. Liu, G. Zhang, Determining the micro-fracture properties of Antrim gas shale by an improved micro-indentation method, Journal of Natural Gas Science & Engineering, 62 (2019) 224-235.

[51] S. Xu, Y. Feng, J. Liu, Q. Zeng, Micro indentation fracture of cement paste assessed by energy-based method: The method improvement and affecting factors, Construction and Building Materials, 231 (2020) 117136.

[52] M. Liu, C. Lu, A.K. Tieu, Crystal plasticity finite element method modelling of indentation size effect, International Journal of Solids and Structures, 54 (2015) 42-49.

[53] W. Yao, J. You, Berkovich nanoindentation study of monocrystalline tungsten: a crystal plasticity study of surface pile-up deformation, Philosophical Magazine, 97 (2017) 1418-1435.

[54] Y. Li, G. Zhang, Z. Wang, P. Wang, Z. Guan, Integrated experimental-computational approach for evaluating elastic modulus of cement paste corroded in brine solution on microscale, Construction and Building Materials, 162 (2018) 459-469.

[55] M. Le Rouzic, T. Chaussadent, L. Stefan, M. Saillio, On the influence of Mg/P ratio on the properties and durability of magnesium potassium phosphate cement pastes, Cement and Concrete Research, 96 (2017) 27-41.

[56] S. Naderi, M. Hassan, A.R. Bushroa, Alternative methods to determine the elastoplastic properties of sintered hydroxyapatite from nanoindentation testing, Materials & Design, 67 (2015) 360-368.

[57] M. Liu, C. Lu, K.A. Tieu, C.-T. Peng, C. Kong, A combined experimental-numerical approach for determining mechanical properties of aluminum subjects to nanoindentation, Scientific reports, 5 (2015) 15072.

[58] M. Liu, K.A. Tieu, K. Zhou, C.-T. Peng, Indentation analysis of mechanical behaviour of torsion-processed single-crystal copper by crystal plasticity finite-element method modelling, Philosophical Magazine, 96 (2016) 261-273.

[59] A. Karimzadeh, S.S.R. Koloor, M.R. Ayatollahi, A.R. Bushroa, M.Y. Yahya, Assessment of nano-indentation method in mechanical characterization of heterogeneous nanocomposite materials using experimental and computational approaches, Scientific reports, 9 (2019) 1-14.

[60] M. Bird, S.L. Butler, C. Hawkes, T. Kotzer, Numerical modeling of fluid and electrical currents through geometries based on synchrotron X-ray tomographic images of reservoir rocks using Avizo and COMSOL, Computers & Geosciences, 73 (2014) 6-16.

[61] K.L. Scrivener, The use of backscattered electron microscopy and image analysis to study the porosity of cement paste, MRS Online Proceedings Library Archive, 137 (1988).

[62] X. Liu, Y. Li, Plain Concrete Prisms Externally Strengthened by CFRP Bonded with Graphene Oxide–Modified Magnesium Phosphate Cement, Journal of Materials in Civil Engineering, 32 (2020) 04020069.

[63] C.A. Schneider, W.S. Rasband, K.W. Eliceiri, NIH Image to ImageJ: 25 years of image analysis, Nature methods, 9 (2012) 671-675.

[64] T. Nguyen-Sy, T.-K. Nguyen, V.-D. Dao, K. Le-Nguyen, N.-M. Vu, Q.-D. To, T.-D. Nguyen, T.-T. Nguyen, A flexible homogenization method for the effective elastic properties of cement pastes with w/c effect, Cement and Concrete Research, 134 (2020) 106106.

[65] R. Hill, A self-consistent mechanics of composite materials, Journal of the Mechanics and Physics of Solids, 13 (1965) 213-222.

[66] W. Trawiński, J. Bobiński, J. Tejchman, Two-dimensional simulations of concrete fracture at aggregate level with cohesive elements based on X-ray μCT images, Engineering Fracture Mechanics, 168 (2016) 204-226.

[67] X. Wang, M. Zhang, A.P. Jivkov, Computational technology for analysis of 3D meso-structure effects on damage and failure of concrete, International Journal of Solids and Structures, 80 (2016) 310-333.

[68] Z. Wu, W. Cui, L. Fan, Q. Liu, Mesomechanism of the dynamic tensile fracture and fragmentation behaviour of concrete with heterogeneous mesostructure, Construction and Building Materials, 217 (2019) 573-591.

[69] ABAQUS: User's Manual, Version 6.12, Dassault Systèmes Simulia Corp, United States, 2012.

[70] A. Tabiei, W. Zhang, Cohesive element approach for dynamic crack propagation: Artificial compliance and mesh dependency, Engineering Fracture Mechanics, 180 (2017) 23-42.

[71] N. Blal, L. Daridon, Y. Monerie, S. Pagano, Criteria on the artificial compliance inherent to the intrinsic cohesive zone, Comptes Rendus Mécanique, 339 (2011) 789-795.

[72] M. Hlobil, V. Šmilauer, G. Chanvillard, Micromechanical multiscale fracture model for compressive strength of blended cement pastes, Cement and Concrete Research, 83 (2016) 188-202.

[73] W. Ren, Z. Yang, R. Sharma, C. Zhang, P.J. Withers, Two-dimensional X-ray CT image based meso-scale fracture modelling of concrete, Engineering Fracture Mechanics, 133 (2015) 24-39.

[74] X. Wang, Z. Yang, A.P. Jivkov, Monte Carlo simulations of mesoscale fracture of concrete with random aggregates and pores: a size effect study, Construction and Building Materials, 80 (2015) 262-272.

[75] C.M. López, I. Carol, A. Aguado, Meso-structural study of concrete fracture using interface elements. I: numerical model and tensile behavior, Materials and structures, 41 (2008) 583-599.

[76] B.A. Young, A. Hall, L. Pilon, P. Gupta, G. Sant, Can the compressive strength of concrete be estimated from knowledge of the mixture proportions?: New insights from statistical analysis and machine learning methods, Cement and Concrete Research, 115 (2019) 379-388.

[77] R. Cai, T. Han, W. Liao, J. Huang, D. Li, A. Kumar, H. Ma, Prediction of surface chloride concentration of marine concrete using ensemble machine learning, Cement and Concrete Research, 136 (2020) 106164.

[78] E. Gomaa, T. Han, M. ElGawady, J. Huang, A. Kumar, Machine learning to predict properties of fresh and hardened alkali-activated concrete, Cement and Concrete Composites, (2020) 103863.

Graphical abstract

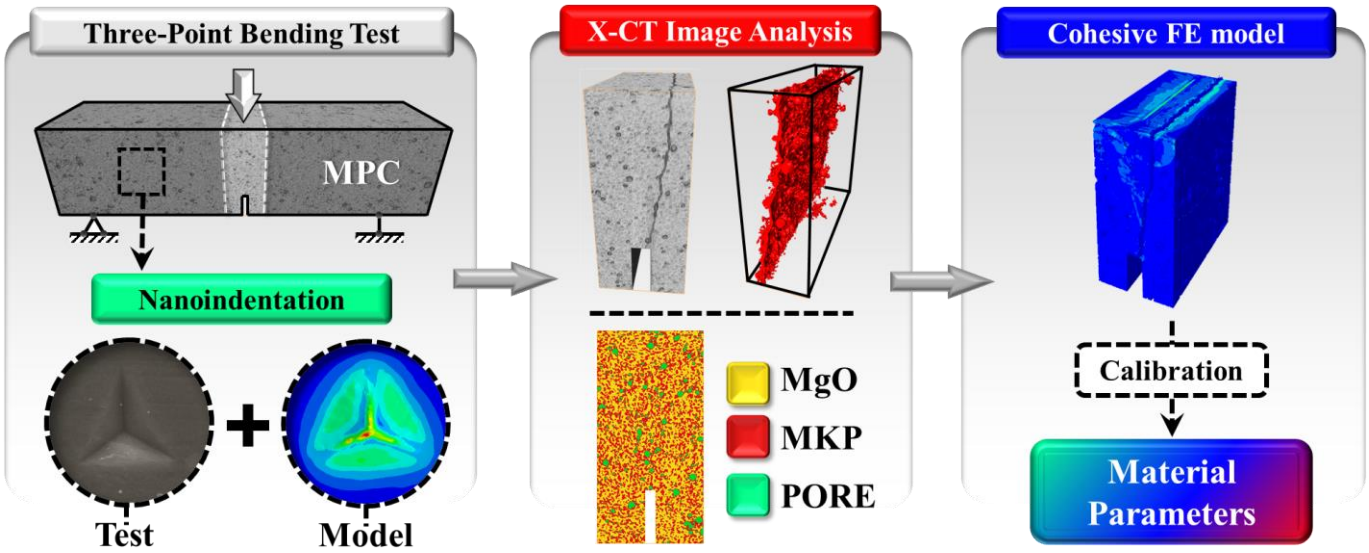

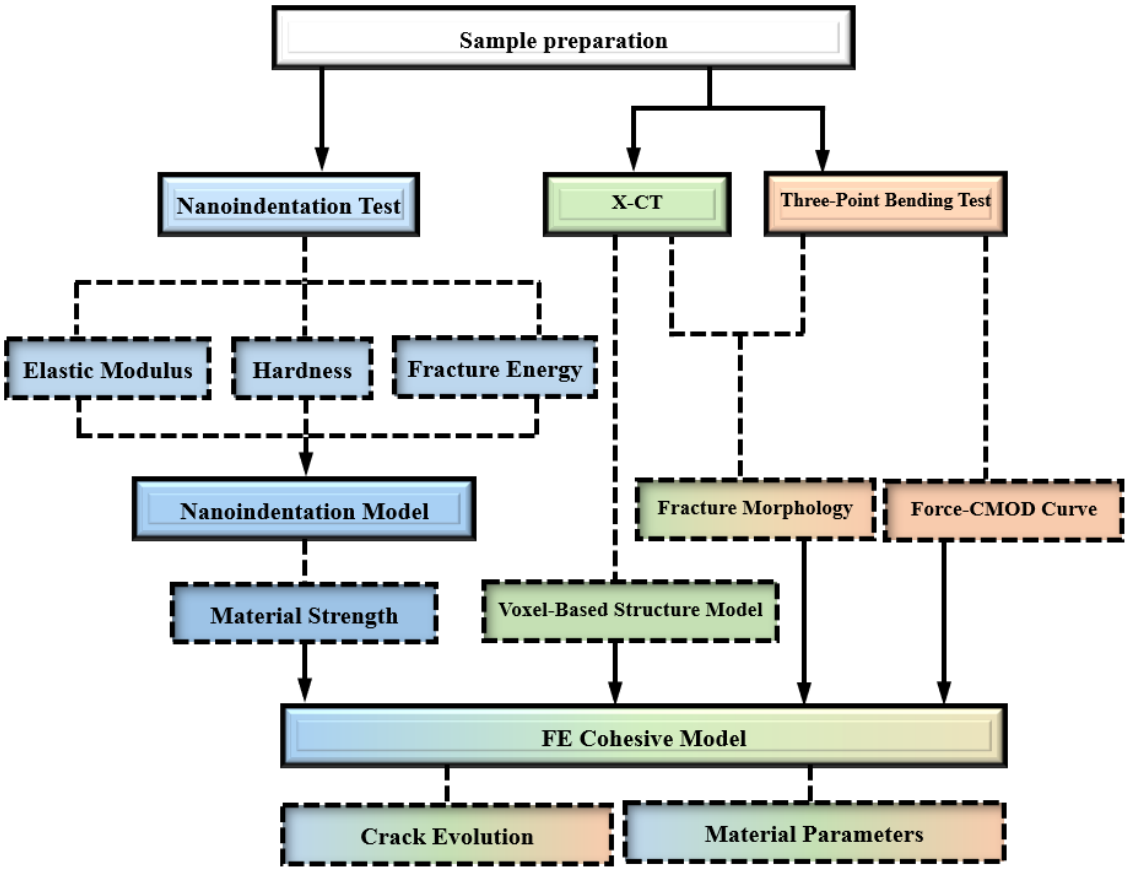

Fig. 1. An overview of the developed experimental-modelling methodology to determine mechanical properties of magnesium phosphate cement (MPC).

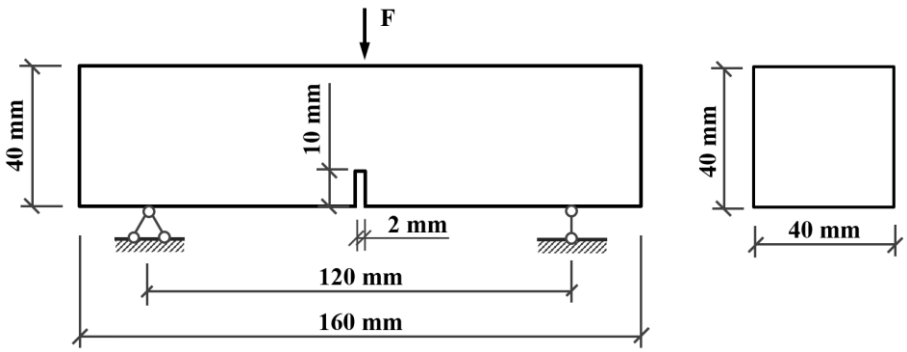

Fig. 2. Dimensions of the notched specimen used for three-point bending test.

Fig. 3. MPC sample sealed with epoxy for nanoindentation test.

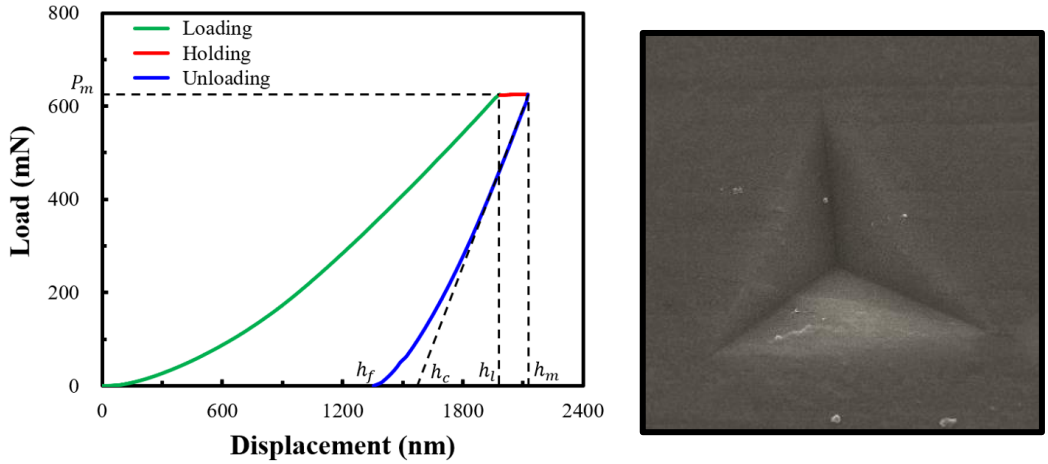

Fig. 4. (a) An example of indentation load-displacement curve and (b) the SEM image for IR_{MgO_3}.

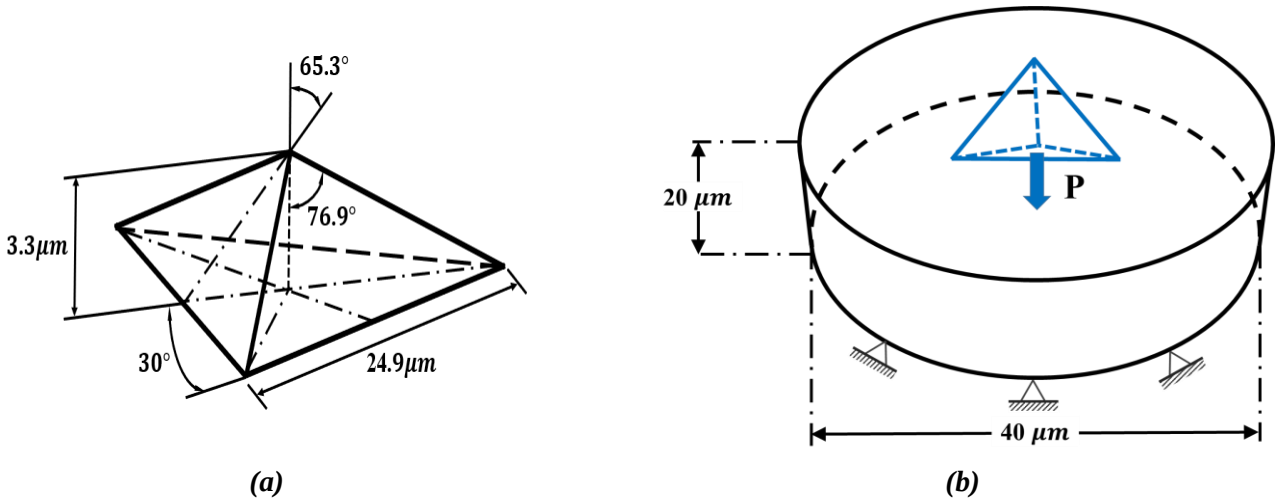

Fig. 5. (a) Dimensions of the Berkovich indenter and (b) boundary conditions applied in the nanoindentation model.

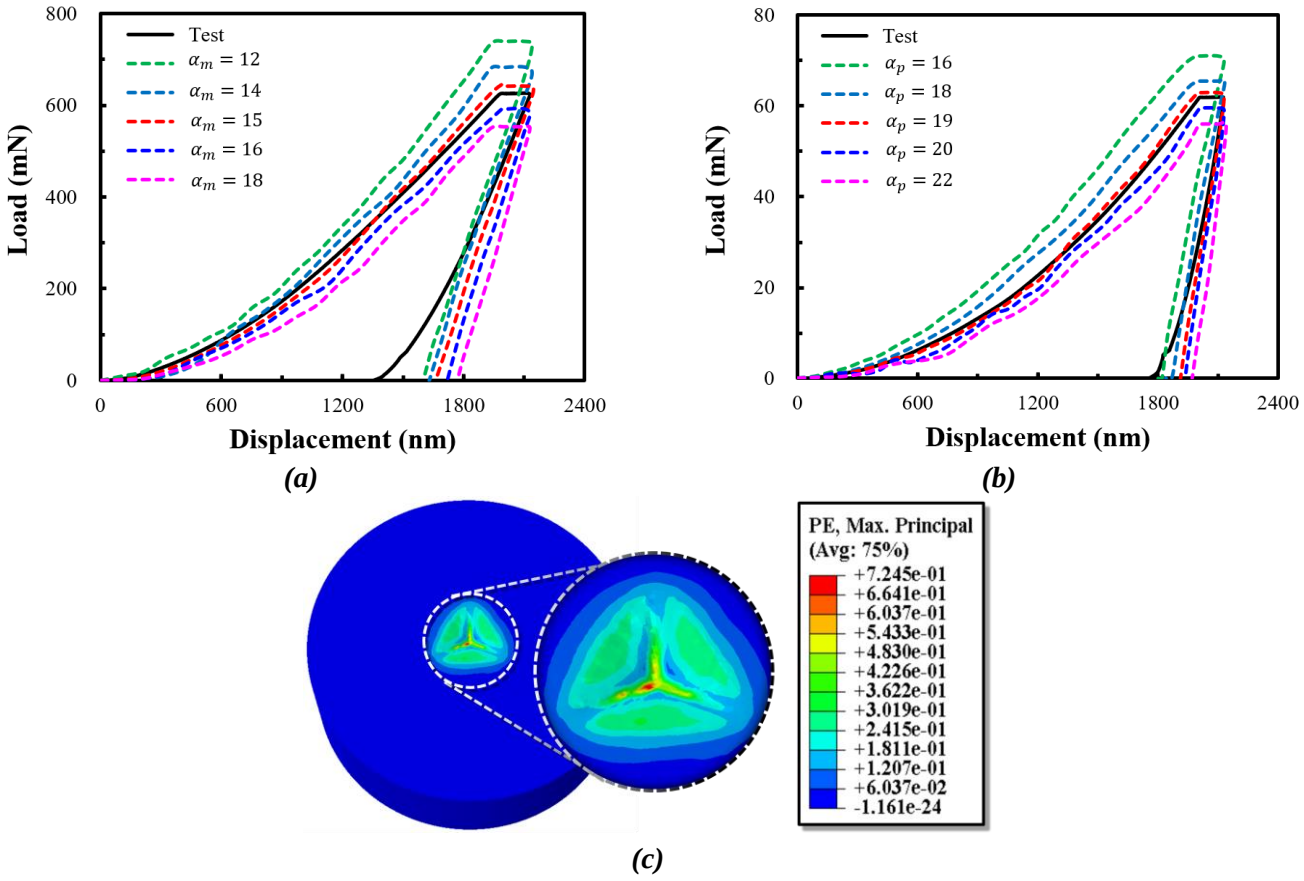

Fig. 6. Simulation results of the nanoindentation test: indentation load-displacement curves for different values of parameter α for (a) MgO model and (b) MKP model; (c) deformation of MgO sample after the indentation process.

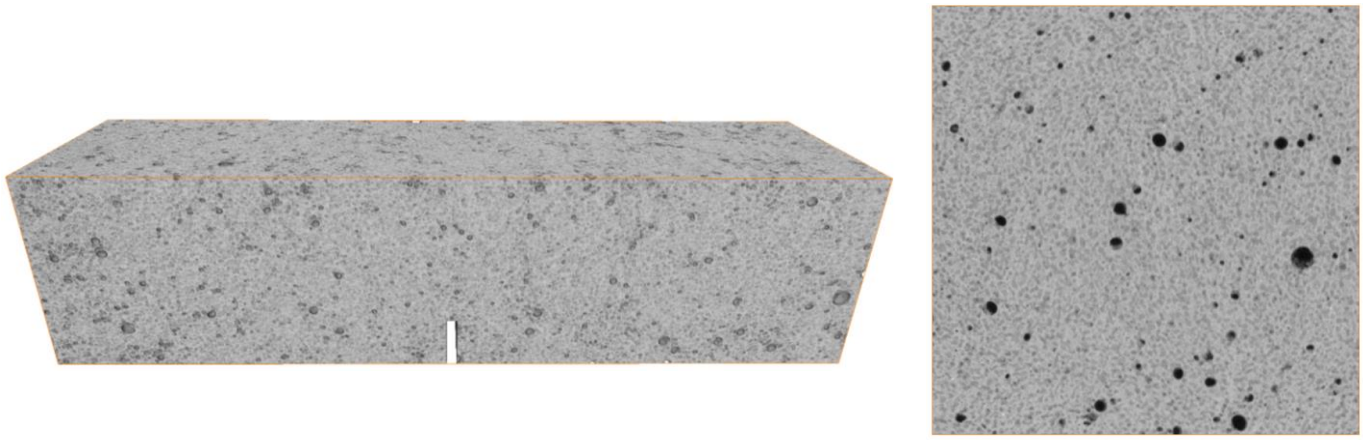

Fig. 7. (a) Reconstructed 3D XCT image of the beam sample and (b) an example of 2D slice image.

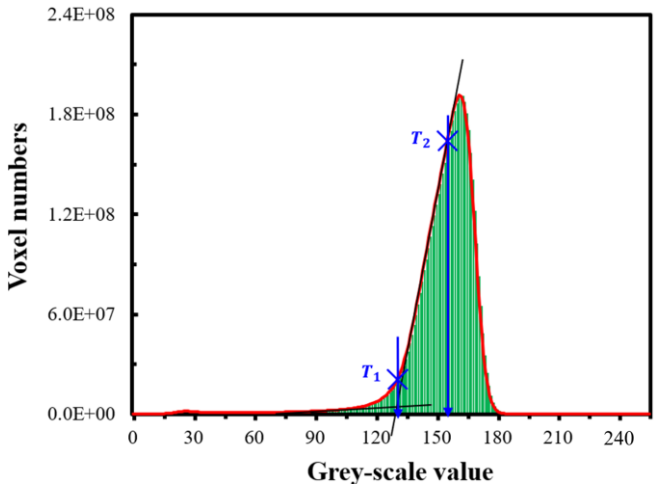

Fig. 8. Grey level histogram of the reconstructed XCT image.

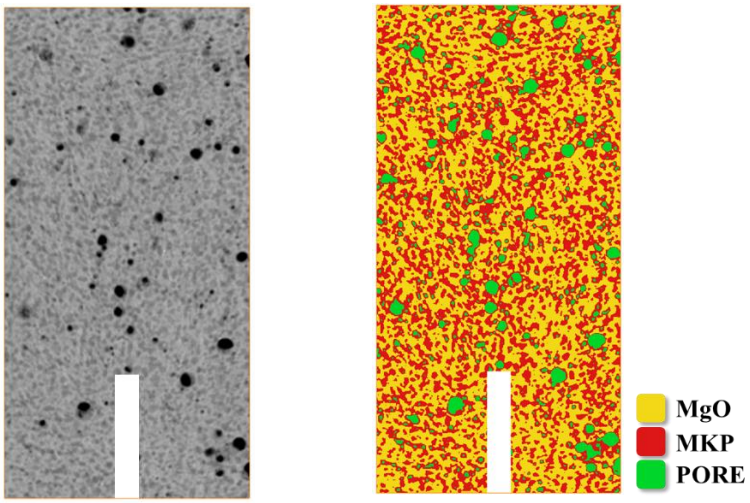

Fig. 9. 2D XCT image (a) before and (b) after the segmentation process.

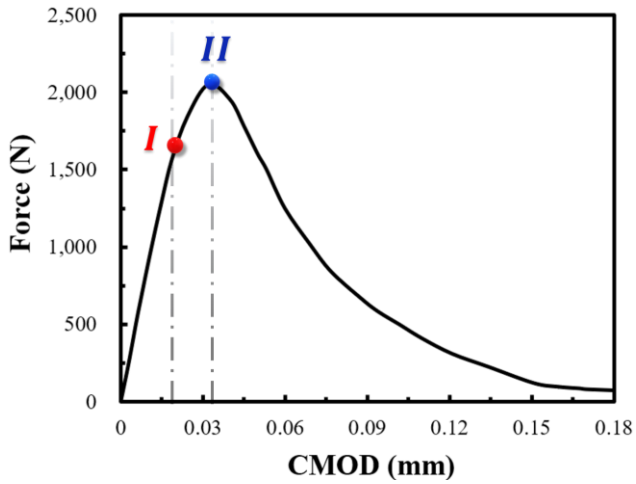

Fig. 10. Force-CMOD (crack mouth opening displacement) curve obtained from three-point bending test on the notched MPC specimen.

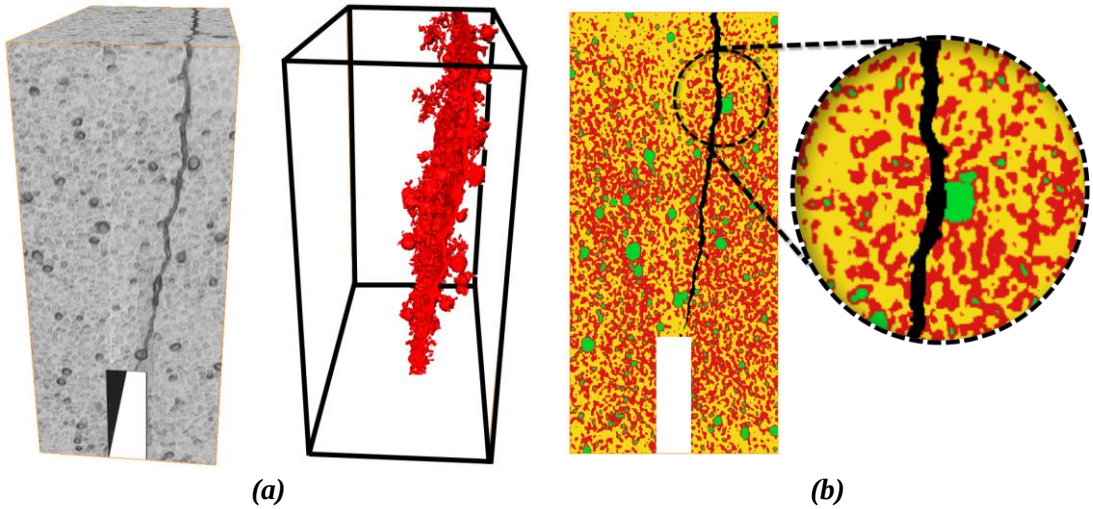

Fig. 11. Final crack morphology in the ROI after bending test: (a) the reconstructed 3D image of the sample and (b) the 2D XCT image after segmentation.

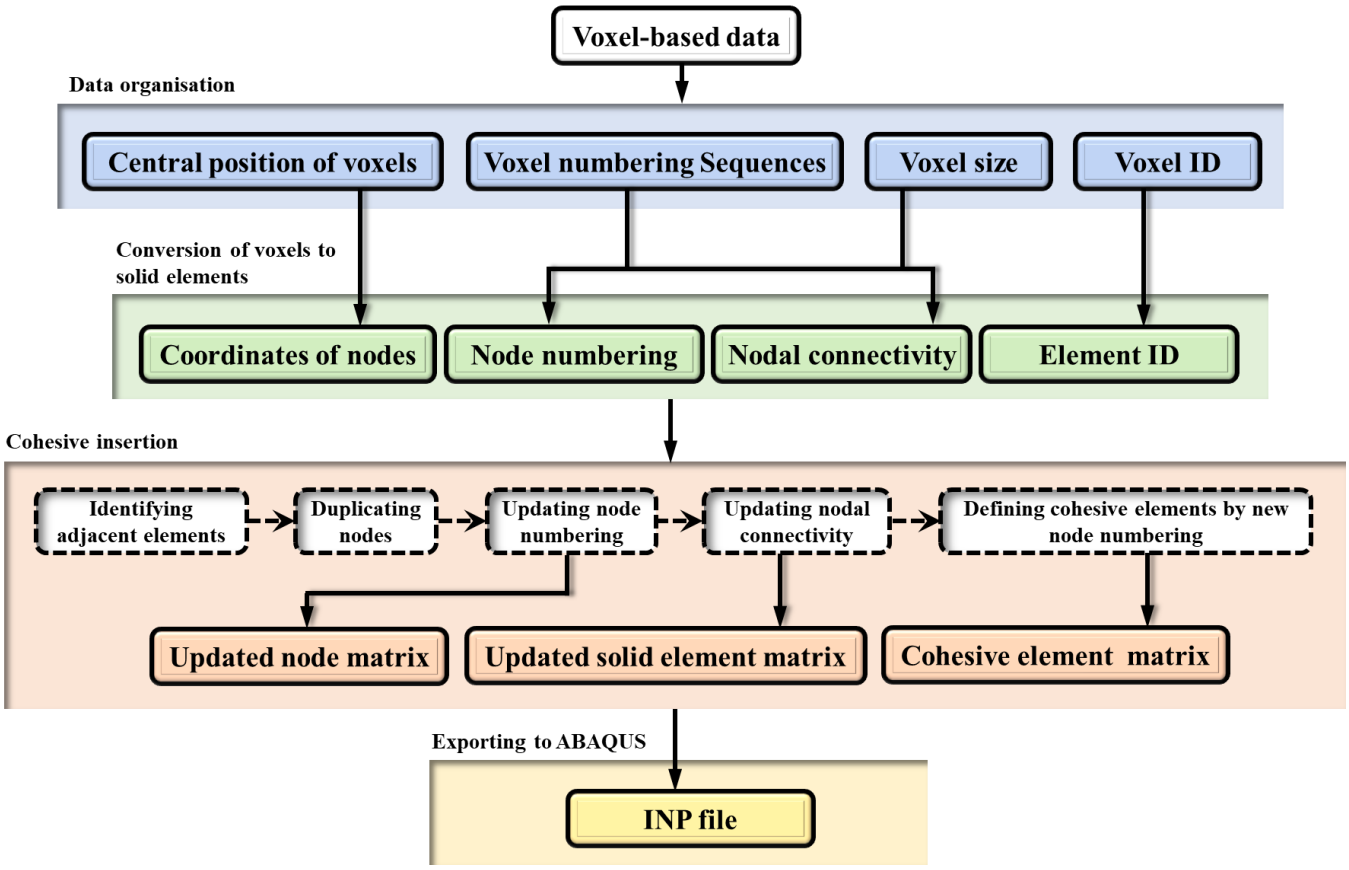

Fig. 12. Main steps of the algorithm to generate meso-structure mesh.

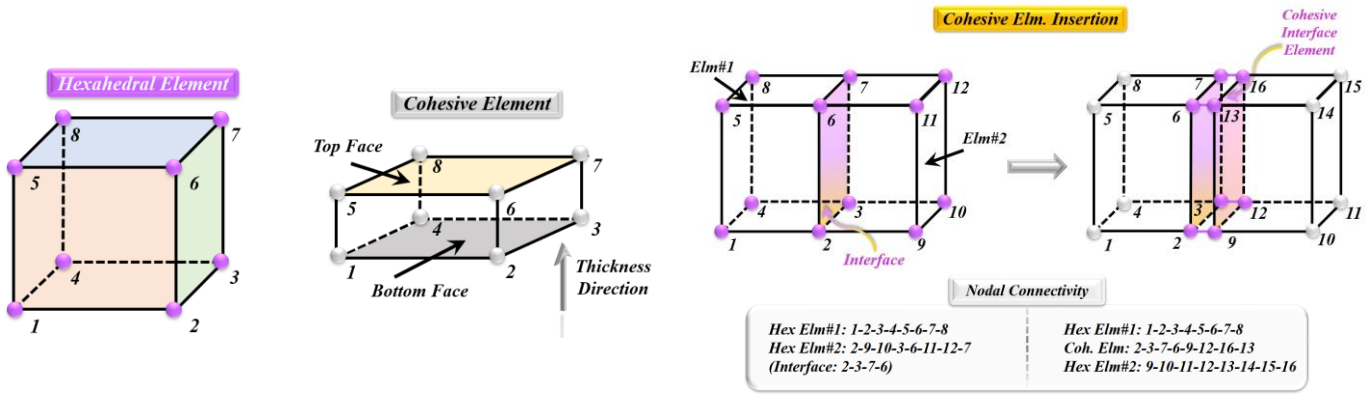

Fig. 13. (a) Node numbering for hexahedral and cohesive elements and (b) inserting a cohesive element at the interface of two hexahedral elements.

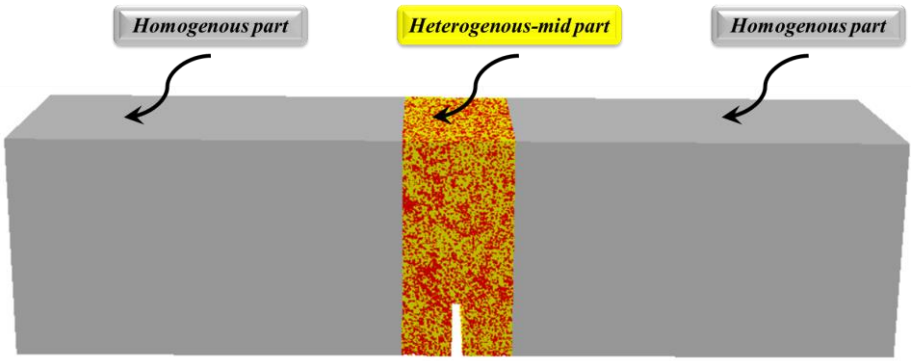

Fig. 14. Beam composition in the FE model.

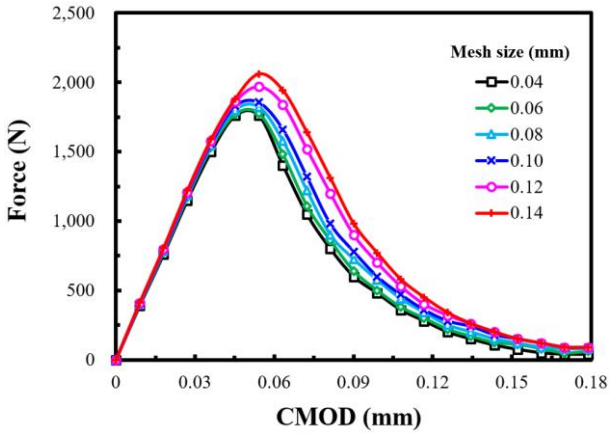

Fig. 15. Simulated force-CMOD curves for different mesh sizes.

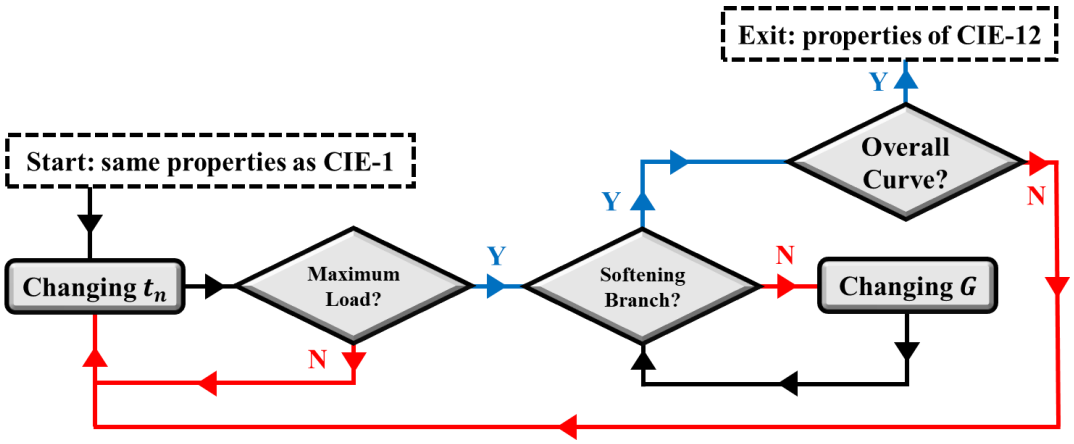

Fig. 16. Model calibration algorithm to characterise the material parameters for CIE-12.

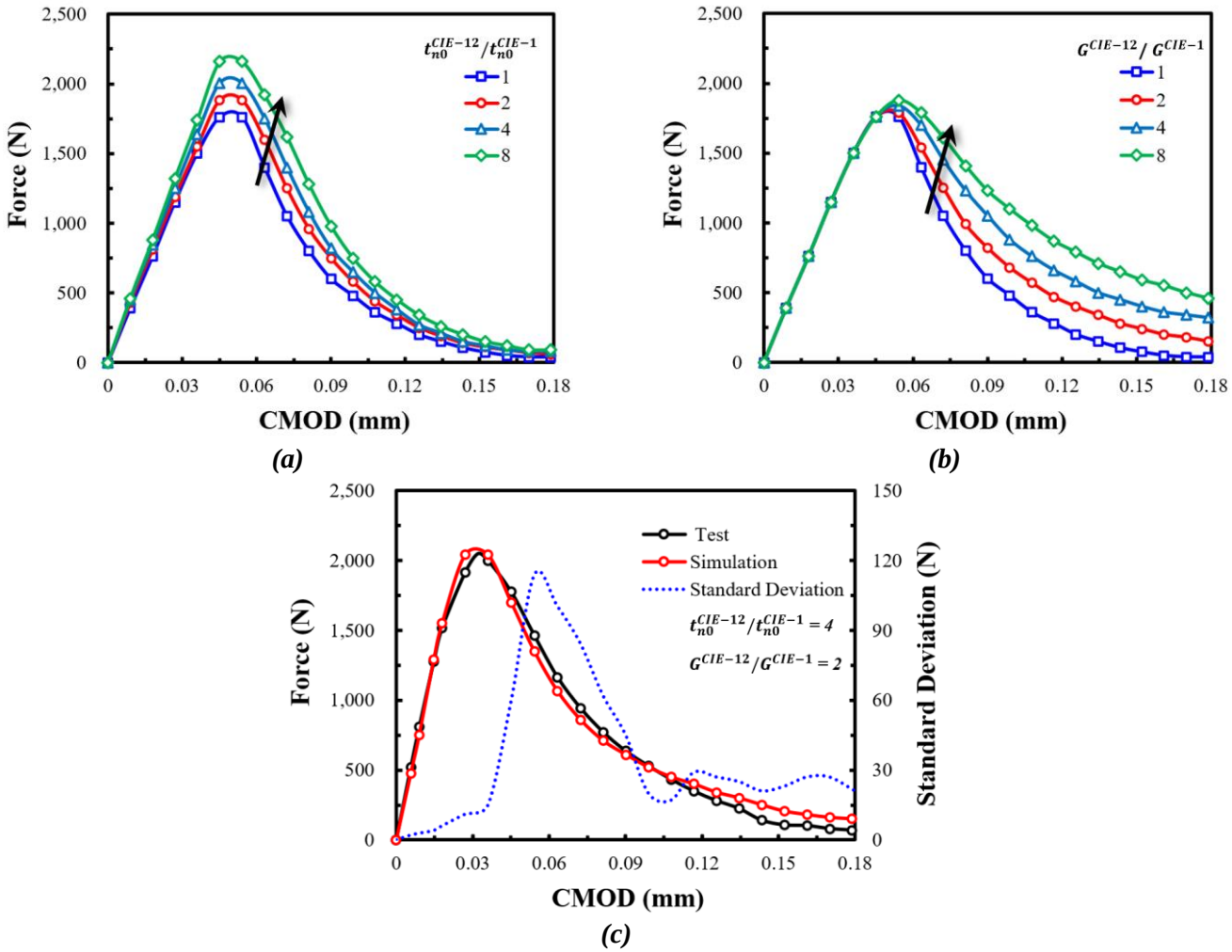

Fig. 17. Effects of (a) t_{n0} and (b) G assigned for the CIE-12 on the load-CMOD curve; (c) simulation results after calibration in comparison with experimental data and standard deviation between them during loading. The arrows are guides for the eyes to show the effect by increasing the ratios.

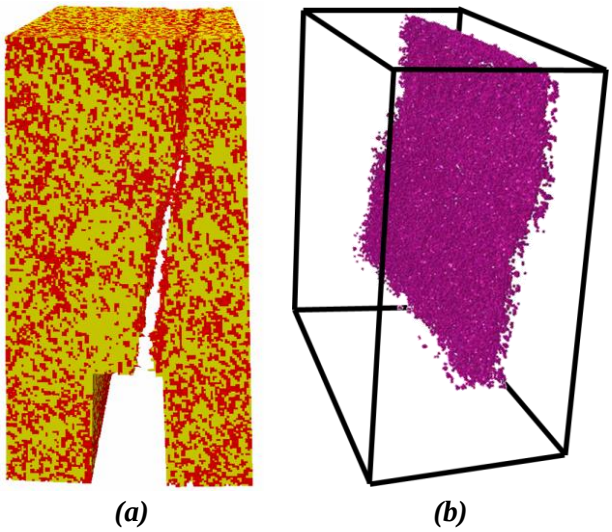

Fig. 18. Simulated final crack morphology in the ROI: (a) the model without the failed CIES and (b) the fracture surface represented with the CIEs with SDEG of 1.

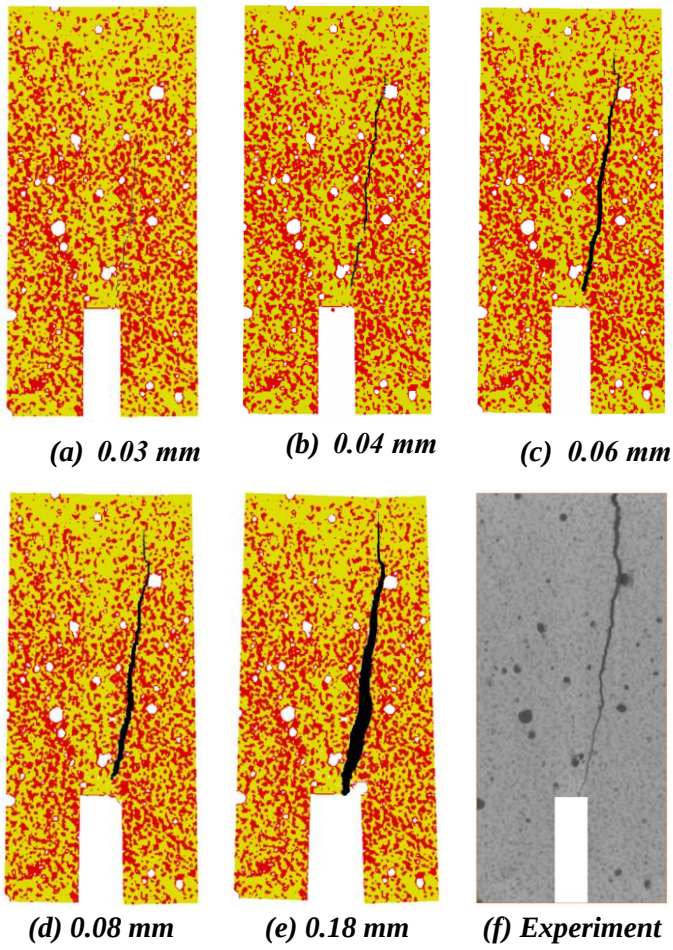

Fig. 19. (a)-(f) Crack growth shown with the cross-sectional view in the ROI (at z = 10 mm) in different vertical displacement and (f) a comparison of simulated and observed cracks.

Table 1. Chemical composition and physical properties of calcined MgO.

Sample	MgO (%)	CaO (%)	SiO_2 (%)	Al_2O_3 (%)	Fe_2O_3 (%)	Density (g/cm^3)	Bulk density (g/cm^3)	Specific surface area (cm^2/g)
MgO	91.7	1.4	1.6	4	1.3	3.46	1.67	805.9

Table 2. MPC proportions.

MgO (g)	KH_2PO_4 (g)	Water (g)	Borax (g)
1140	860	280	57

Table 3. Mechanical properties of MgO obtained from nanoindentation tests and EDS analysis.

Indented region (IR)	Atomic ratio (%) of element		E (GPa)	H (GPa)	G_C (N/m)
	O K	Mg K			
IR_{MgO_1}	48.72	51.28	277.0	15.4	77.7
IR_{MgO_2}	50.33	49.67	273.2	14.9	85.5
IR_{MgO_3}	49.16	50.84	284.5	14.8	74.5
IR_{MgO_4}	49.57	50.43	280.7	16.1	76.1
IR_{MgO_5}	51.78	48.22	308.2	17.5	82.3
IR_{MgO_6}	50.09	49.91	296.4	16.5	81.3
Mean	49.94	50.06	286.7	15.9	79.0

Table 4. Mechanical properties of MKP obtained from nanoindentation tests and EDS analysis.

Indented region (IR)	Atomic ratio (%) of element				E (GPa)	H (GPa)	G_C (N/m)
	O K	Mg K	P K	K K			
IR_{MKP_1}	77.82	7.32	7.56	7.30	33.5	1.4	21.2
IR_{MKP_2}	78.30	7.06	7.33	7.31	29.6	1.0	15.7
IR_{MKP_3}	75.73	8.04	7.96	8.27	24.4	0.9	19.9
IR_{MKP_4}	75.64	8.13	8.25	7.98	33.2	1.3	22.9
IR_{MKP_5}	76.92	7.89	7.76	7.43	28.9	1.2	21.3
IR_{MKP_6}	77.38	7.59	7.38	7.65	27.0	1.1	21.3
Mean	76.97	7.67	7.71	7.66	29.4	1.1	20.4

Table 5. Results of the incorporation of FE analysis and calibration process.

Substrate	α	σ_y (MPa)	Relative error compared to experimental data			
			P_m (%)	h_l (%)	h_m (%)	h_f (%)
MgO	15	1060	2.72	0.35	5.05	19.7
MKP	19	58	2.84	0.18	0.16	8.14

Table 6. A summary of material properties used in the final FE cohesive zone model after the calibration process.

Material properties	Solid Elements		Cohesive Elements		
	MgO	MKP	CIE_1	CIE_2	CIE_12
Young's modulus, E (GPa)	286.7	29.4	-	-	-
Poisson's ratio, ν	0.22	0.18	-	-	-
Density, ρ (kg/m^3)	3540	1864	1864	3540	2702
Elastic stiffness, k_{n0}, k_{s0}, k_{t0} (MPa/mm)	-	-	10^5	10^5	10^5
Cohesive strength, t_n, t_s, t_t (MPa)	-	-	5.8	106	24
Fracture energy, G_c(N/mm)	-	-	0.02	0.079	0.041